iMAP Beamforming for High-Quality High Frame Rate Imaging

Tanya Chernyakova, Dan Cohen, Meged Shoham, and Yonina C. Eldar, *Fellow, IEEE*

***Abstract*— We present a statistical interpretation of beamforming to overcome the limitations of standard delay-and-sum (DAS) processing. Both the interference and the signal of interest are viewed as random variables, and the distribution of the signal of interest is exploited to maximize the *a posteriori* distribution of the aperture signals. In this formulation, the beamformer output is a maximum *a posteriori* (MAP) estimator of the signal of interest. We provide a closed-form expression for the MAP beamformer and estimate the unknown distribution parameters from the available aperture data using an empirical Bayes approach. We propose a simple scheme that iterates between the estimation of distribution parameters and the computation of the MAP estimator of the signal of interest, leading to an iterative MAP (iMAP) beamformer. This results in a suppression of the interference compared with DAS, without a severe increase in computational complexity or the need for fine-tuning of parameters. The effect of the proposed method on contrast is studied in detail and measured in terms of contrast ratio (CR), contrast-to-noise ratio (CNR), and contrast-to-speckle ratio (CSR). By implementing iMAP on both simulated and experimental data, we show that only 13 transmissions are required to obtain a CNR comparable to DAS with 75 plane waves. Compared to other interference suppression methods, such as coherence factor and scaled Wiener processing, iMAP shows an improved contrast and a better preserved speckle pattern.**

***Index Terms*— Adaptive beamforming, array signal processing, ultrasonic imaging.**

I. Introduction

B-MODE ultrasound imaging can be performed using numerous insonification strategies varying from focused beams to plane-wave and diverging-wave transmissions. Narrow transmissions improve signal-to-noise ratio (SNR) and spatial resolution, while broad unfocused insonification accelerates image acquisition, leading to ultrafast imaging methods [1]. The signals detected by the transducer elements after transmission include reflections from the entire insonified area. To determine the value of a B-mode image at a certain point, focusing delays are applied on the signals in an attempt to isolate an on-target echo originating from this point.

Manuscript received May 4, 2019; accepted July 26, 2019. Date of publication August 6, 2019; date of current version November 21, 2019. This work was supported by the European Union's Horizon 2020 Research and Innovation Program under Grant 646804-ERC-COG-BNYQ. *(Corresponding author: Tanya Chernyakova.)*

T. Chernyakova was with the Department of Electrical Engineering, Technion—Israel Institute of Technology, Haifa 3200003, Israel. She is now with Vayyar Imaging Ltd., Yahud, Israel (e-mail: ctanya@campus.technion.ac.il).

D. Cohen and M. Shoham are with the Department of Electrical Engineering, Technion—Israel Institute of Technology, Haifa 3200003, Israel.

Y. C. Eldar is with the Faculty of Mathematics and Computer Science, Weizmann Institute of Science, Rehovot 7610001, Israel.

Digital Object Identifier 10.1109/TUFFC.2019.2933506

In the most common delay-and-sum (DAS) beamforming, the delayed signals are simply averaged to yield the signal of interest. Due to the finite aperture size, the off-target echoes are not entirely suppressed by averaging. As a result, a DAS beampattern is characterized by the main lobe width and levels of sidelobes. Another source of clutter is phase aberrations originating from sound speed inhomogeneities. Together with reverberation echoes produced by impedance mismatches, they further reduce the contrast of a DAS image. These limitations are especially prominent for wide transmissions, where due to lack of transmit focus, clutter originates from a much wider insonified area. Several approaches have been proposed to overcome these limitations of DAS beamforming.

A. Related Work

The sidelobe level of a DAS beamformer can be controlled by weighting the aperture elements. When constant, i.e., signal independent, weights are applied, this process is referred to as fixed apodization and reduces sidelobes at the expense of a wider main lobe, degrading the lateral resolution. This tradeoff can be avoided by using adaptive weights, computed based on the detected signals.

Minimum variance (MV) beamforming [2] improves the resolution without sacrificing contrast by computing the adaptive weights based on estimated signal statistics. Its application to ultrasound imaging was studied extensively over the last two decades [3]–[8]. The need to estimate and invert the data covariance matrix per each image point makes MV beamforming computationally intensive and creates a bottleneck for real-time implementation.

Another approach for clutter suppression assumes that the signal originating at the focal point is highly coherent over the aperture elements while the interference is not. Based on this assumption, a coherence factor (CF) [9], [10] is calculated as a ratio of coherent to incoherent sums across the signals detected by the aperture to multiply the beamformer output [11]–[16]. Despite the advantages of CF combined with either DAS or MV beamforming, the resulting images may suffer from reduced image brightness and degraded speckle pattern, especially in a low SNR. A detailed study of this phenomenon is presented in [17], where CF is analyzed in the context of Wiener beamforming [18] and its calculation is interpreted in terms of estimation of signal and noise power. Several alternatives including a scaled Wiener (ScW) postfilter are proposed by Nilsen and Holm [17] to provide a tradeoff between contrast improvement and robustness to low SNR and are studied for focused acquisition.

Methods based on unfocused insonification, such as plane-wave imaging, can potentially highly benefit from CF processing to improve contrast. In this mode, the quality of an image is inherently reduced due to low SNR and the lack of transmit focus. The latter implies that the clutter originates from a much wider area and severely reduces the contrast of the image. By coherently compounding data obtained by transmitting several tilted plane waves, the image quality is improved and is proportional to the number of transmissions [19]. The latter should be kept as low as possible to maintain a high frame rate and reduce the number of computations leading to a tradeoff between the image quality and the frame rate.

The application of CF processing for broad insonification is challenging due to decreased accuracy in the coherent sum estimation [16]. Several works propose to apply CF-based methods coupled with variations in MV beamforming to overcome this problem [16], [20]. However, the implementation of MV processing for ultrafast imaging is prohibitive computationally.

B. Contributions

In this work, we present a statistical interpretation of beamforming leading to an alternative framework for processing the detected signals. In the proposed approach, both the interference and the signal of interest are viewed as random variables. This allows exploiting the distribution of the signal of interest in order to maximize the *a posteriori* distribution of signals detected by the aperture. In this formulation, the beamformer output is a maximum *a posteriori* (MAP) estimator of the signal of interest. We provide a closed-form expression for the MAP beamformer, which depends on the signal of interest and the interference distribution parameters. Since the latter are unknown, we estimate them from the available aperture data using an empirical Bayes approach [21]. We propose a simple scheme that iterates between the estimation of distribution parameters using maximum likelihood (ML) and the computation of the MAP estimator, leading to an iterative MAP (iMAP) beamformer.

To put the proposed method in context, we review Wiener beamforming, Wiener postfilter, CF, and ScW processing and the relationship between them [12], [13], [17]. We also discuss different strategies for statistics estimation used by these methods and compare them with the ML approach used by iMAP.

We consider simulated, experimental, and *in vivo* data sets provided on the PICMUS website [22] to show that iMAP beamforming with one and two iterations, referred to as iMAP1 and iMAP2, provides a significant improvement in interference suppression compared with DAS, without affecting the resolution for any number of transmissions. The effect of the proposed method and other interference suppression techniques on contrast is studied in detail and measured in terms of contrast ratio (CR), contrast-to-noise ratio (CNR), and contrast-to-speckle ratio (CSR). We show that iMAP1 requires only 13 plane waves to obtain a CNR comparable to that of DAS with 75 transmissions. We also compare iMAP with Wiener postfilter, CF, and ScW with statistics estimation suggested in [17]. The results show that the proposed method provides improved contrast for simulated, experimental, and *in vivo* data sets. Finally, the effect of iMAP and other interference suppression methods on speckle is assessed by evaluating the statistics of the resulting images. Our tests show the improved preservation of speckle patterns by our approach.

The rest of the article is organized as follows. We introduce the signal model and present iMAP beamforming in Sections II and III, respectively. CF, Wiener, and ScW processing and their connection to the proposed method are reviewed in Section IV. The experimental setup and results are presented in Sections V–VII. A discussion on contrast improvement and metrics appears in Section VIII.

II. Signal Model and Standard Processing

We consider a linear array of M elements. The delays are applied to the signals received by the elements after transmission, either focused or broad, to focus the array to a point of interest (r, θ) upon reception. These delayed signals are referred to as aperture data. The analysis is performed for each given image point; therefore, the indexes r and θ are omitted in the following derivations. The delayed signal at the mth element is

$$y_m = x + n_m \tag{1}$$

where x is a signal of interest that represents the reflectivity of the underlying image at the focal point (r, θ), and n_m stands for an additive interference including the off-target reflections, aberration and reverberation clutter, and system noise. In vector notation, (1) becomes

$$\mathbf{y} = x\mathbf{1} + \mathbf{n} \tag{2}$$

where the vector $\mathbf{y}$ corresponds to the aperture data, $\mathbf{1}$ is a vector of ones, and $\mathbf{n}$ is the interference vector. All the vectors are of length M.

The two most common beamforming techniques for array processing are DAS and MV. Standard DAS beamforming maximizes the output energy in the direction of interest, namely, the foresight. It reduces to recover the signal of interest by averaging the aperture data, that is,

$$x_{\mathrm{DAS}} = \frac{1}{M}\sum_{m=1}^{M} y_m = \frac{1}{M}\mathbf{1}^H\mathbf{y}. \tag{3}$$

MV beamforming [2] maintains a unity gain in the foresight while minimizing the energy received from other directions

$$\min_{\boldsymbol{w}} E[|\boldsymbol{w}^H\mathbf{y}|^2] \quad \text{s.t.} \quad \boldsymbol{w}^H\mathbf{1} = 1. \tag{4}$$

Assuming that the data vector $\mathbf{y}$ has a correlation matrix $\mathbf{R}_y = E[\mathbf{y}\mathbf{y}^H]$, the optimal weights are given by

$$\boldsymbol{w}_{\mathrm{MV}} = \frac{\mathbf{R}_y^{-1}\mathbf{1}}{\mathbf{1}^H\mathbf{R}_y^{-1}\mathbf{1}}. \tag{5}$$

The implementation of the MV beamformer requires estimation and inversion of the data correlation matrix per each image point [5], [6]. As a result, computational complexity

is increased and is often prohibitive for real-time implementation. In addition, image quality is sensitive to estimation errors so that strategies such as spatial smoothing and diagonal loading are required to improve robustness. This introduces parameters that have to be tuned for every specific application.

The formulation in (2) implies that the aperture data can be viewed as M noisy measurements of the signal of interest x. The interference vector $\mathbf{n}$ accounts for several phenomena. It includes acquisition noise, as well as phase aberrations and reverberation echoes. The latter stems from tissue inhomogeneity and high impedance mismatches that can occur at tissue boundaries, e.g., fat and muscle tissue intersection characterized by high- and low-speed velocities may trap ultrasound signals and generate reverberation clutter [23]. All the above can be naturally assumed to be spatially white. Another interference source, the off-target reflections, produces correlated clutter at transducer elements when focused transmission is considered. In this case, the insonified area is relatively narrow and corresponds to the main lobe and major sidelobes of the transmitted beampattern. A reflector located there affects the receive elements in a correlated way. For broad unfocused transmissions, such as plane and diverging waves, the insonified region is much wider. As a result, the off-target clutter at each element is a superposition of numerous reflections originating in the insonified area. Due to the diversity of geometric paths from the insonified reflectors to each one of the elements, the spatial correlation is reduced. We, therefore, assume that the overall interference at the elements is spatially white, namely, independent and identically distributed (i.i.d.) Gaussian. Explicitly

$$\mathbf{n} \sim N\left(\mathbf{0}, \sigma_n^2 \mathbf{I}\right) \tag{6}$$

where $\mathbf{I}$ is the $M \times M$ identity matrix, and σ_n^2 is the noise variance. Further assumptions on x imply the processing that should be applied on the measurement vector $\mathbf{y}$ to recover the signal of interest.

Suppose, first, that x is a deterministic unknown parameter. The ML estimate of x is then given by

$$\begin{aligned} x_{\mathrm{ML}} &= \arg\max_x p(\mathbf{y}; x) \\ &= \frac{1}{M}\mathbf{1}^H\mathbf{y} = \frac{1}{M}\sum_{m=1}^{M} y_m \end{aligned} \tag{7}$$

where $(\cdot)^H$ stands for the Hermitian operator. Thus, under the assumption of uncorrelated Gaussian noise at the aperture elements, the ML estimator corresponds to the output of standard DAS beamforming given in (3).

To allow for more involved processing, we consider x to be a random variable and use MAP estimation to recover it from the noisy measurements.

III. MAP Beamforming

A. MAP Estimator

Suppose, next, that the signal of interest is a Gaussian random variable with variance σ_x^2, $x \sim N(0, \sigma_x^2)$, uncorrelated with the noise. We can then consider an MAP estimator

$$x_{\mathrm{MAP}} = \arg\max_x p(\mathbf{y}|x)\, p(x). \tag{8}$$

Since $\mathbf{y}|x \sim N(x\mathbf{1}, \sigma_n^2\mathbf{I})$ and $x \sim N(0, \sigma_x^2)$, the MAP estimator of x is given by

$$x_{\mathrm{MAP}} = \frac{\sigma_x^2}{\sigma_n^2 + M\sigma_x^2}\mathbf{1}^H\mathbf{y} = \frac{M\sigma_x^2}{\sigma_n^2 + M\sigma_x^2}x_{\mathrm{DAS}}. \tag{9}$$

The beamformer weights are correspondingly

$$\boldsymbol{w}_{\mathrm{MAP}} = \frac{\sigma_x^2}{\sigma_n^2 + M\sigma_x^2}\mathbf{1}. \tag{10}$$

The expression in (9) implies that the summation of the aperture data in MAP beamforming is performed using weights defined by the parameters of the prior distribution of the signal of interest and the interference. In most realistic scenarios, the parameters are unknown and, therefore, need to be estimated from the data at hand. This leads to the iMAP beamformer, which we introduce next.

B. Prior Distribution Parameter Estimation

To estimate the unknown parameters σ_x^2 and σ_n^2, we use an empirical Bayes approach [21]. Specifically, given σ_x^2 and σ_n^2, x can be estimated using (9). On the other hand, for a given realization of x and $\mathbf{y}$, the unknown parameters can be estimated using an ML approach

$$\left\{\hat{\sigma}_x^2, \hat{\sigma}_n^2\right\}_{\mathrm{ML}} = \arg\max_{\sigma_x^2, \sigma_n^2} p\left(\mathbf{y}, x; \sigma_x^2, \sigma_n^2\right) \tag{11}$$

with

$$\begin{aligned} p(\mathbf{y}, x; \sigma_x^2, \sigma_n^2) &= \left(2\pi\sigma_x^2\right)^{-\frac{1}{2}} \exp\left\{-\frac{x^2}{2\sigma_x^2}\right\} \\ &\quad \times \left(2\pi\sigma_n^2\right)^{-\frac{M}{2}} \exp\left\{-\frac{1}{2\sigma_n^2}||\mathbf{y} - x\mathbf{1}||^2\right\}. \end{aligned} \tag{12}$$

This results in

$$\begin{aligned} \hat{\sigma}_x^2 &= x^2 \\ \hat{\sigma}_n^2 &= \frac{1}{M}||\mathbf{y} - x\mathbf{1}||^2. \end{aligned} \tag{13}$$

We thus suggest iterating between (9) and (13) so as to use the signal of interest to improve the estimation of the distribution parameters and vice versa. The resulting beamformer is presented in Algorithm 1. The only parameters required by the proposed method are the initialization of x and stopping criteria.

In Algorithm 1, we use the DAS beamformer as an initial guess for x. The number of iterations can be chosen, e.g., according to the desired contrast value. However, defining such a value is practical only for predefined phantoms, where the true values of the underlying image are known. Thus, a more practical approach is to define the number iterations empirically. We found experimentally that the second iteration of iMAP leads to about 80–100-dB noise suppression inside the cyst regions. Since the typical dynamic range of medical ultrasound varies from 60 to 80 dB, such a noise suppression is sufficient and further iterations are unnecessary. We, therefore, considered only two iterations in all the following examples.

Algorithm 1 iMAP Beamforming

1: Initialize $\hat{x}_{(0)} = \frac{1}{M}\mathbf{1}^H\mathbf{y}$.
2: For current estimate $\hat{x}_{(t)}$ use (13) to compute

$$\left\{\hat{\sigma}_x^2, \hat{\sigma}_n^2\right\}_{(t)} = \left\{\hat{x}_{(t)}^2, \frac{1}{M}\left\|\mathbf{y} - \hat{x}_{(t)}\mathbf{1}\right\|^2\right\}.$$

3: Given $\{\hat{\sigma}_x^2, \hat{\sigma}_n^2\}_{(t)}$ use (9) to update

$$\hat{x}_{(t+1)} = \frac{\hat{\sigma}_{x,(t)}^2}{\hat{\sigma}_{n,(t)}^2 + M\hat{\sigma}_{x,(t)}^2}\mathbf{1}^H\mathbf{y}.$$

4: Iterate 2 and 3 until stopping criterion is met.

IV. Comparison With Related Methods

In this section, we review CF scaling, Wiener beamforming, and Wiener postfilter, and focus on the relationship between them following derivations in [17]. We then compare ScW, a generalization of Wiener processing proposed in [17], with iMAP beamforming.

A. Coherence Factor

The CF [9], [10] is computed as a ratio of coherent to incoherent sums across the aperture signals. For a given range, CF is defined by

$$\mathrm{CF} = \frac{\left|\sum_{m=1}^{M} y_m\right|^2}{M\sum_{m=1}^{M}|y_m|^2} = \frac{|\mathbf{1}^H\mathbf{y}|^2}{M\mathbf{y}^H\mathbf{y}}. \tag{14}$$

In [12] and [13], CF is used as a scaling factor multiplying the output of DAS. Assuming that the signal originating at the focal point is highly coherent over the aperture elements while the interference is not, multiplication by CF suppresses the off-target echoes and improves contrast. The resulting value of the B-mode image at the point of interest is

$$x_{\mathrm{CF}} = \mathrm{CF}\cdot x_{\mathrm{DAS}} \tag{15}$$

with x_{DAS} given by (3). A significant contrast improvement is reported in [12] also for the cases with phase distortions stemming from focusing imperfections of different kinds. Despite the advantages of CF, the resulting images may suffer from reduced image brightness and degraded speckle pattern, especially in the low SNR regime.

B. Wiener Processing

For the Gaussian model assumed in this work, MAP estimation is equivalent to minimizing the mean-squared error (MSE). Explicitly, $\boldsymbol{w}_{\mathrm{MAP}}$ is also the solution to the problem

$$\min_{\boldsymbol{w}} E[|x - \boldsymbol{w}^H\mathbf{y}|^2] \tag{16}$$

and, therefore, can be referred to as Wiener beamforming [18]. Nilsen and Holm [17] studied Wiener processing to provide a theoretical basis for performance and limitations of CF. In their work, they present a derivation of Wiener beamforming and propose the concept of a Wiener postfilter for any distortionless beamformer. The signal of interest is assumed to be independent of additive zero-mean interference; however, no assumptions are made on the statistics of the interference. In particular, it is not assumed to be spatially white.

For this general case, the Wiener beamformer that solves (16) is given by [17]

$$\boldsymbol{w}_{\mathrm{wiener}} = \frac{E[x^2]}{E[x^2] + \boldsymbol{w}_{\mathrm{MV}}^H\mathbf{R}_n\boldsymbol{w}_{\mathrm{MV}}}\boldsymbol{w}_{\mathrm{MV}} \tag{17}$$

where $\mathbf{R}_n = E[\mathbf{n}\mathbf{n}^H]$ and $\boldsymbol{w}_{\mathrm{MV}}$ is the MV beamformer of (5). Thus, the implementation of the general Wiener beamformer has the same drawbacks as MV beamforming discussed in Section II.

It can be seen from (17) that the Wiener beamformer is an MV beamformer scaled by a factor defined by the ratio of the signal power to the total power of the MV beamformer output. Based on this, Nilsen and Holm [17] define the Wiener postfilter as a scaling factor that can be found for any beamformer $\boldsymbol{w}$ satisfying $\boldsymbol{w}^H\mathbf{1} = 1$ to minimize the MSE

$$\begin{aligned} H_{\mathrm{wiener}} &= \arg\min_{H} E[|x - H\boldsymbol{w}^H\mathbf{y}|^2] \\ &= \frac{E[x^2]}{E[x^2] + \boldsymbol{w}^H\mathbf{R}_n\boldsymbol{w}}. \end{aligned} \tag{18}$$

Implementing H_{wiener} requires the estimation of $E[x^2]$ and $\mathbf{R}_n$ and does not involve matrix inversion. To implement a Wiener postfilter for a DAS beamformer, namely, for $\boldsymbol{w} = \boldsymbol{w}_{\mathrm{DAS}}$, the following estimators are proposed in [17]:

$$\begin{aligned} \hat{E}[x^2] &= x_{\mathrm{DAS}}^2 \\ \hat{\mathbf{R}}_n &= \frac{1}{K}\sum_{k=1}^{K}(\mathbf{y}_k - x_{\mathrm{DAS}}\mathbf{1})(\mathbf{y}_k - x_{\mathrm{DAS}}\mathbf{1})^H \end{aligned} \tag{19}$$

with $\mathbf{y}_k = [y_k, \ldots, y_{k+L-1}]$. The estimator of $\mathbf{R}_n$, therefore, is computed by applying spatial smoothing, i.e., by dividing the total aperture of length M to overlapping subarrays of length L and averaging their covariance matrices.

Under the assumption of spatially white interference in (6), i.e., $\mathbf{R}_n = \sigma_n^2\mathbf{I}$, the Wiener beamformer in (17) coincides with the Wiener postfilter for a DAS beamformer and is given by

$$\begin{aligned} \boldsymbol{w}_{\mathrm{wiener}} &= H_{\mathrm{wiener}}\boldsymbol{w}_{\mathrm{DAS}} \\ &= \frac{E[x^2]}{E[x^2] + \frac{1}{M}\sigma_n^2}\frac{1}{M}\mathbf{1} \\ &= \frac{E[x^2]}{M\cdot E[x^2] + \sigma_n^2}\mathbf{1}. \end{aligned} \tag{20}$$

For $x \sim N(0, \sigma_x^2)$, (20) becomes

$$\boldsymbol{w}_{\mathrm{wiener}} = H_{\mathrm{wiener}}\boldsymbol{w}_{\mathrm{DAS}} = \frac{\sigma_x^2}{M\sigma_x^2 + \sigma_n^2}\mathbf{1} \tag{21}$$

and is equivalent to the MAP beamformer.

C. Scaled Wiener Postfilter and iMAP

To pinpoint the relationship between the CF and Wiener beamforming, Nilsen and Holm [17] rewrite (14) as

$$\begin{aligned}\mathrm{CF} &= \frac{\left|\sum_{m=1}^{M} y_m\right|^2}{M\sum_{m=1}^{M}|y_m|^2} \\ &= \frac{\left|\frac{1}{M}\mathbf{1}^H\mathbf{y}\right|^2}{\left|\frac{1}{M}\mathbf{1}^H\mathbf{y}\right|^2 + \frac{1}{M}\left||\mathbf{y}-\frac{1}{M}\mathbf{1}^H\mathbf{y}\mathbf{1}\right|\right|^2} \\ &= \frac{|x_{\mathrm{DAS}}|^2}{|x_{\mathrm{DAS}}|^2 + \frac{1}{M}||\mathbf{y}-x_{\mathrm{DAS}}\mathbf{1}||^2}.\end{aligned} \tag{22}$$

For the case of spatially white interference, $|x_{\mathrm{DAS}}|^2$ and $\frac{1}{M}||\mathbf{y}-x_{\mathrm{DAS}}\mathbf{1}||^2$ can be viewed as the estimators of the signal and noise power, i.e., $\hat{\sigma}_x^2$ and $\hat{\sigma}_n^2$, respectively. This allows for the following interpretation of the CF output:

$$x_{\mathrm{CF}} = \frac{\mathrm{CF}}{M}\mathbf{1}^H\mathbf{y} = \frac{\sigma_x^2}{M\sigma_n^2 + M\sigma_x^2}\mathbf{1}^H\mathbf{y}. \tag{23}$$

Comparing (21) with (23), CF may be interpreted as a Wiener postfilter for a DAS beamformer with overestimated noise variance [17]. The overestimation of noise results in more severe suppression of the beamformer output, leading on the one hand to improved contrast, but on the other, to reduced image brightness and degraded speckle patterns.

To combine contrast improvement obtained by CF with the robustness of Wiener processing, preserving image brightness and speckle, the following heuristic solution, referred to as an ScW postfilter, is proposed in [17]:

$$x_{\mathrm{ScW}} = \frac{\sigma_x^2}{\alpha\sigma_n^2 + M\sigma_x^2}\mathbf{1}^H\mathbf{y}. \tag{24}$$

Choosing α in the range from 1 to M, one can gradually move from Wiener to CF performance. To implement the ScW, Nilsen and Holm [17] use the following estimators:

$$\begin{aligned}\hat{\sigma}_x^2 &= |x_{\mathrm{DAS}}|^2 \\ \hat{\sigma}_n^2 &= \frac{1}{M}||\mathbf{y}-x_{\mathrm{DAS}}\mathbf{1}||^2\end{aligned} \tag{25}$$

which correspond to the ML estimators in (13) used for the first iteration of iMAP. We note that for $\alpha = 1$ and estimators in (25), ScW is equivalent to the first iteration of iMAP. However, ScW with $\alpha = 1$ was not studied and verified experimentally in [17]. To the best of our knowledge, this work is the first to provide such results, referred in the context of this article as iMAP1.

We note that, theoretically, Wiener processing should provide an optimal solution in terms of MSE. The fact that CF yields improved contrast compared with Wiener beamforming and Wiener postfilter, as reported in [17], can be explained by poor estimation of σ_x^2 and σ_n^2. The estimator of σ_x^2 used for Wiener processing

$$\hat{\sigma}_x^2 = |x_{\mathrm{DAS}}|^2 \tag{26}$$

overestimates the energy of the true signal since it includes all the interference that is not suppressed by DAS beamforming. This, in turn, leads to underestimated noise power because of the subtraction of the estimated signal of interest

$$\hat{\sigma}_n^2 = \frac{1}{M}||\mathbf{y}-x_{\mathrm{DAS}}\mathbf{1}||^2. \tag{27}$$

The introduction of α in (24) may be viewed as an attempt to compensate for the estimation flaws in a heuristic way.

The iterative approach proposed in Section III-B deals with the same problem of parameter estimation. Instead of arbitrary compensation for limited estimation accuracy, it uses the available estimator of the signal of interest to improve the estimation of the parameters and vice versa. Thus, we expect it to provide a better performance, as we will demonstrate in Section VII.

V. Experimental Setup

To verify the performance of the proposed method, we used PICMUS data sets [22]. The above include simulated and experimental data as well as *in vivo* acquisitions and are provided at the PICMUS website[1]. The availability of the data together with the detailed description of the proposed method makes the results easily reproducible.

The performance of iMAP1 and iMAP2 is compared with the following methods:

1) DAS beamforming defined in (3);
2) Wiener postfilter for DAS beamformer according to (18) using the estimators in (19);
3) ScW processing according to (24) with estimators in (25) and $\alpha = M^{1/2}$ as proposed in [17];
4) CF using the definition in (14).

The difference between the Wiener postfilter as defined in (18) and iMAP1 is in the way they estimate the interference covariance matrix. The iMAP1 relies on the assumption of spatially white interference, which is not exploited in (19). The comparison of iMAP1 and Wiener postfilter may, thus, provide valuable insight regarding the noise statistics. As mentioned in Section IV-C, ScW can be viewed as a heuristic way to compensate for the statistical estimation flaws. It is compared with iMAP2, which threats the same problem in an iterative fashion.

A. Description of the Data Sets

To study the performance of the proposed method, we use the following data sets.

1) *Simulated Images:* We start with two acquisitions, simulated with Field II [24], [25]. First, we evaluate resolution using a point-reflector phantom with isolated scatterers distributed in an anechoic background. Then, we proceed to contrast evaluation using a simulated phantom of a number of anechoic cysts embedded in speckle.
2) *Experimental Data Set:* Both resolution and contrast are next evaluated experimentally using a recorded data set of a CIRS Multi-Purpose Ultrasound Phantom (Model 040GSE). The scan region contains anechoic cysts and a point reflector.

[1] https://www.creatis.insa-lyon.fr/Challenge/IEEE_IUS_2016/

3) *In Vivo Acquisitions:* Finally, we apply the proposed method on two *in vivo* data sets of a carotid artery. This allows for the qualitative assessment of the proposed technique.

B. Acquisition Parameters

Both simulations and experimental acquisitions are performed with a 128-element probe with λ spacing and central frequency of 5.2 MHz. More details are available on the PICMUS website. Each image acquisition (both simulated and experimental) includes the transmission of 75 plane waves with steering angles spaced uniformly between $-16°$ and $16°$. The results obtained by each one of 75 transmissions are stored and allow for evaluation of an image comprised of an arbitrary number of plane waves. The acquisition is performed with an f-number of 1.75, and no apodization is applied upon reception.

VI. Performance Evaluation

To study the performance of iMAP and compare it with other methods, we evaluate resolution and contrast, which are the major parameters of interest in ultrasound imaging. We also verify the ability of iMAP to preserve the speckle pattern, which is known to be of high value in many medical imaging modalities [26], [27].

A. Resolution

The resolution is evaluated by computing the full-width at half-maximum of the point spread function in the axial and lateral directions.

B. Contrast

When evaluating the performance of iMAP in terms of contrast, we encountered several metrics, established in the literature. The first one is the CR, the ratio between the mean value of the region of interest, cyst in our case, and that of the background [12], [28]

$$\mathrm{CR} = \mu_b - \mu_c \tag{28}$$

where μ_b and μ_c stand for the mean log compressed intensity of the background and the anechoic cyst region, respectively.

CSR, another well-established metric, considers the variances of the background and the region of interest, σ_b^2 and σ_c^2 [29], respectively,

$$\mathrm{CSR} = \frac{\mu_c - \mu_b}{\sqrt{\sigma_c^2 + \sigma_b^2}}. \tag{29}$$

Finally, CNR is defined as the ratio between the CR and the standard deviation of the image intensity in the background, σ_b, [30]

$$\mathrm{CNR} = \frac{\mu_c - \mu_b}{\sigma_b}. \tag{30}$$

This metric evaluates the contrast relative to the background variance and imposes a penalty on methods increasing the variance of the background. CNR is insensitive to the variance in the region of interest, which can be beneficial when the region of interest is an anechoic cyst. Assuming that the mean value within the cyst is significantly reduced compared with background, e.g., tens of decibels, the increased variance of the cyst might not be noticeable in the image. Imposing a penalty for increased variance within the cyst in this case is less informative. CNR defined in (30) is used in [12], [13], and [17] to evaluate the performance of CF, Wiener postfilter, and ScW.

One can expect the three above-mentioned metrics to be correlative. Namely, if one method outperforms another in one of the metrics, it will be superior in all the others as well. However, as we will see in Section VII, this is not always true for the methods discussed in this article. We compute the three above-mentioned metrics to provide a comprehensive study on the performance of the proposed method and related techniques.

C. Speckle Pattern

To compare the effect of iMAP and other interference suppression techniques on speckle, we evaluated the speckle area within the images obtained by different methods. For each image, we performed a Kolmogorov–Smirnov (K-S) test to find the regions obeying a Rayleigh probability density function (pdf) [31], [32]. The K-S test is a common statistical hypothesis test that verifies whether there is enough evidence in data to deduce that the hypothesis under consideration is correct. In our case, the hypothesis is that the investigated pattern obeys the Rayleigh pdf. To this end, the envelope data of each image are divided into overlapping patches of 20×15 pixels and the K-S test is applied to each patch. The patches that pass the K-S test with the significance level $\alpha = 0.05$ are included into the speckle region of each image. The patches that did not pass the test are zeroed out. To quantify the similarity, we define the speckle region of the DAS image as a reference and compute what percentage of it is defined as speckle in images obtained by other techniques.

VII. Results

A. Simulations

1) Resolution: We start with an image of a point-reflector phantom obtained by the simulation of a single plane-wave transmission. Fig. 1 presents the results of DAS, Wiener postfilter, iMAP1 , iMAP2, ScW, and CF. The axial and lateral resolutions are computed as an average over all point reflectors within the image. The resulting values are summarized in Table I. The lateral cross section of a middle point reflector located at a depth of 20 mm is shown in Fig. 3. It can be seen that CF provides the most prominent improvement in both axial and lateral resolutions. All the other methods lead to results that are better or comparable to the standard DAS processing. As is evident in Figs. 1 and 2, the main effect of all the methods is in reduction of the lateral sidelobes, which, as will be shown in Section VII-A2, is expressed in contrast enhancement.

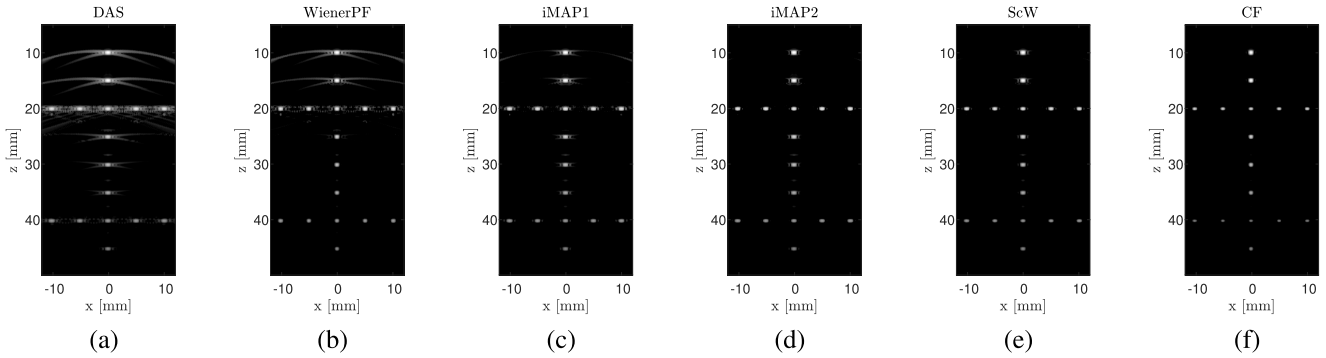

Fig. 1. Images of simulated point-reflector phantom obtained by (a) DAS, (b) Wiener postfilter, (c) iMAP1, (d) iMAP2, (e) ScW, and (f) CF. The dynamic range of all the images is 50 dB.

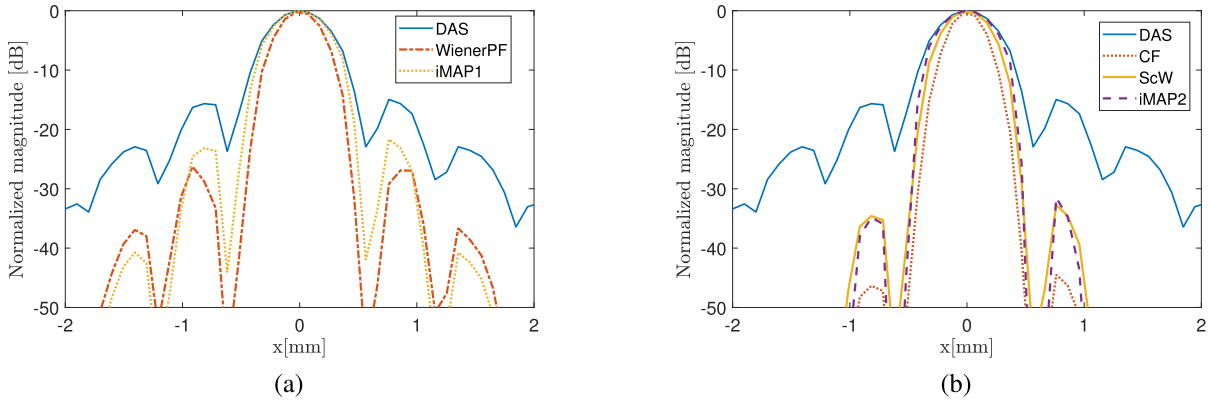

Fig. 2. Lateral cross section of point reflector located at a depth of 20 mm at $x = 0$ mm from Fig. 1. (a) DAS, Wiener postfilter, and iMAP1. (b) DAS, CF, ScW, and iMAP2.

TABLE I
MEASURED AXIAL AND LATERAL RESOLUTIONS

Method	Axial res.[mm]	Lateral res. [mm]
DAS	0.4	0.74
Wiener PF	0.4	0.53
iMAP1	0.4	0.7
ScW	0.37	0.6
CF	0.33	0.44
iMAP2	0.4	0.69

TABLE II
MEASURED CR, CNR, AND CSR

Method	CR [dB]	CNR [dB]	CSR [dB]
DAS	18.8	2.6	1.9
Wiener PF	27.1	1.8	1.3
iMAP1	39.2	3.0	1.8
ScW	44.9	2.8	1.9
CF	46.9	2.7	1.9
iMAP2	86.4	3.1	1.8

2) Contrast: To evaluate contrast obtained by iMAP compared with other techniques, we use an anechoic cyst phantom. Fig. 3 shows the images obtained with DAS, Wiener postfilter, iMAP1, iMAP2, ScW, and CF and gives a qualitative impression of the contrast resulting from each approach. The lateral cross section of three cysts located at a depth of 30 mm is shown in Fig. 4. The acquisition is performed with a single plane-wave transmission. To evaluate the contrast quantitatively, we computed the CR, CNR, and CSR of an image as an average CR, CNR, and CSR over all nine cysts of the simulated phantom, respectively. The resulting values are presented in Table II.

First, we take a closer look at the iMAP1 performance compared with the Wiener postfilter. It can be seen in Fig. 4(a) that iMAP1 provides better interference suppression within the cyst while being closer to DAS result in the speckle regions compared with the Wiener postfilter. These results are confirmed by the values of CR and CNR as given in Table II. As mentioned in Section V, the difference between the Wiener postfilter and the iMAP1 is in the estimation of the noise covariance matrix. The superior performance of iMAP1 compared with Wiener postfilter, thus, may be explained by poor estimation of the latter. The estimator of $\mathbf{R}_n$ in (19) does not consider an assumption of spatially white noise. This assumption is used by iMAP and leads to improved performance. This provides empirical justification for the spatially white interference model used in this work.

We next compare the results of CF, ScW, and iMAP2. All these techniques are characterized by a very sharp magnitude dropoff at the transition from speckle to cyst regions, as shown in Fig. 4(b). As a result, cyst boundaries in Fig. 3 are very clear even for an image obtained with a single plane-wave

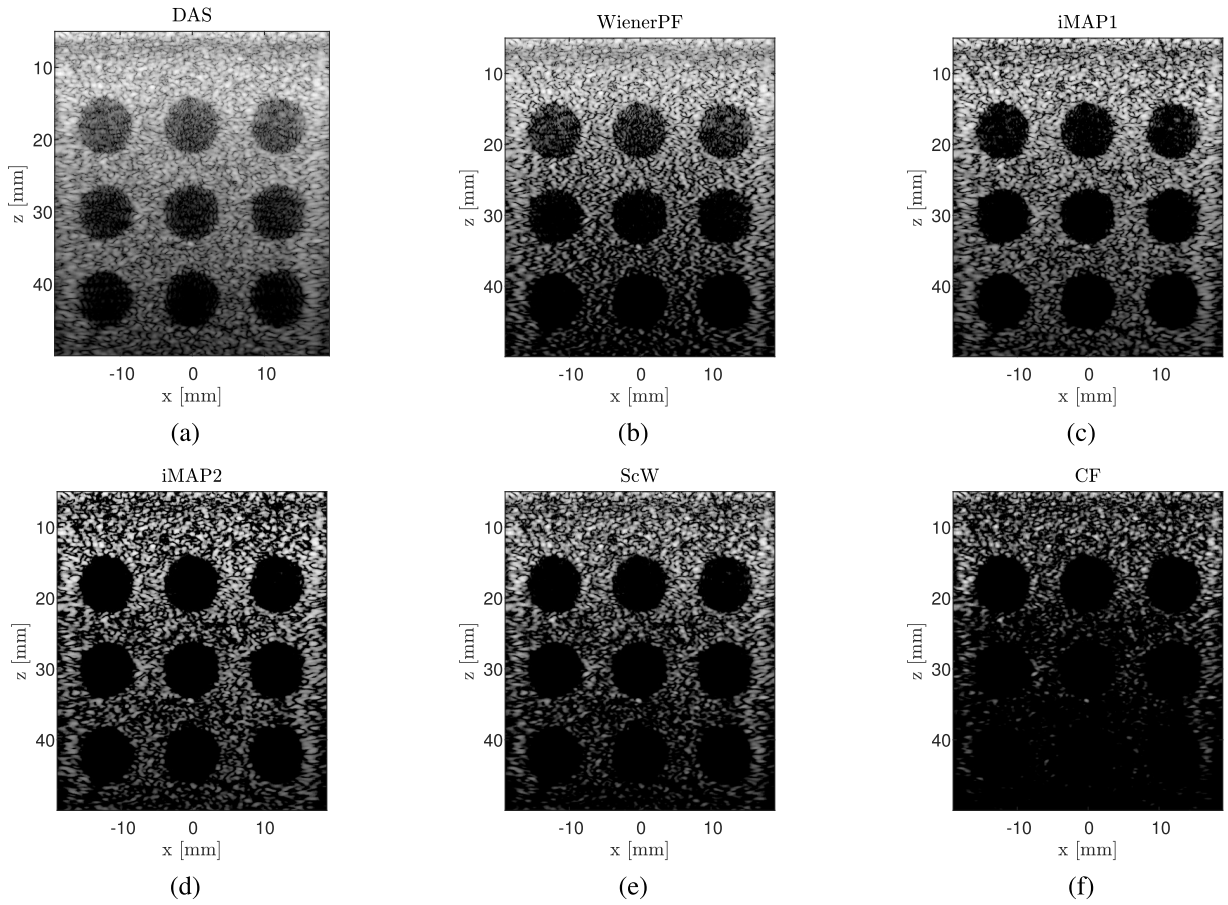

Fig. 3. Images of simulated anechoic cyst phantom obtained by (a) DAS, (b) Wiener postfilter, (c) iMAP1, (d) iMAP2, (e) ScW, and (f) CF. The dynamic range for all the images is 60 dB.

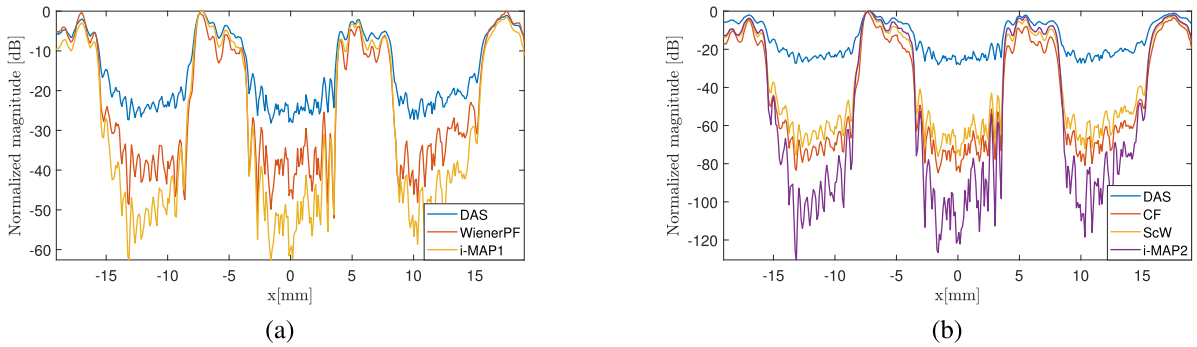

Fig. 4. Lateral cross section of three cysts located at a depth of 30 mm from Fig. 3. (a) DAS, Wiener postfilter, and iMAP1. (b) DAS, CF, ScW, and iMAP2.

transmission. As expected, an image obtained by CF suffers from severely reduced brightness. Even though noise within the cyst is highly suppressed, leading to increased CR, the improvement in CNR obtained by CF is moderate due to reduced brightness and higher variance of the surrounding area. The performance of ScW is improved compared with CF. Visually, the resulting image resembles the one obtained by iMAP2; however, the values of both CR and CNR for iMAP2 are higher. Fig. 4(b) shows that iMAP2 outperforms both CF and ScW in terms of noise suppression within the cyst. Despite the superior noise suppression, the effect of iMAP2 within the speckle regions is less prominent compared with CF and ScW. This shows that iMAP2 does not suppress the magnitude uniformly over all image regions and has better adaptive capabilities compared with CF and ScW.

In terms of CR and CNR, iMAP1 and iMAP2 are superior compared with the Wiener postfilter and CF and ScW, respectively. We also note that all the above-mentioned methods, except Wiener postfilter, outperform DAS. However, the values of CSR for all interference suppressing methods, studied in this article, are comparable or even lower than DAS. This is

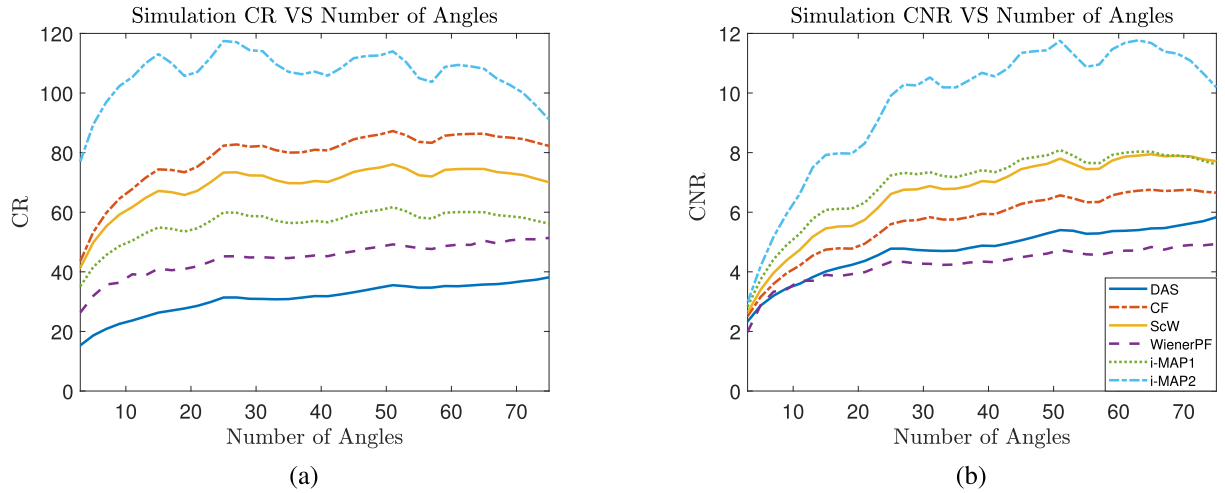

Fig. 5. (a) CR and (b) CNR as a function of the number of transmitted plane waves.

explained by the increased variance within the cyst region, σ_c^2, which is penalized by CSR. The increase in variance is clearly seen in the cyst lateral cross section in Fig. 4. However, its effect on the resulting images in Fig. 3 is less prominent due to the significantly reduced mean value within the cyst compared with the background.

We also note that there is a difference between the performance improvement in terms of CR and CNR for all the methods being studied. The CR is increased by up to four times, e.g., iMAP2 compared with DAS, while the improvement in CNR is much more moderate. The inconsistency in contrast metrics is discussed in detail in Section VIII.

3) Contrast for Multiple Plane-Wave Transmissions: To evaluate the performance of different methods for the transmission of multiple plane waves with different inclinations, we present the CR and CNR as a function of the number of transmitted plane waves, varying from 3 to 75. The angles are spaced uniformly between $-16°$ and $16°$ to keep the lateral resolution comparable for a different number of plane waves. As shown in Fig. 5, the CR and CNR increase with the number of transmitted plane waves for all the approaches. In terms of CR, iMAP1 outperforms the Wiener postfilter, while iMAP2 provides better results compared with CF and ScW. In terms of CNR, iMAP for both one and two iterations outperforms other methods being studied. iMAP1 provides on average 2.17-dB improvement compared with DAS. For iMAP2, the average improvement is 4.82 dB. For CF and ScW, the average improvement is 0.91 and 1.84 dB, respectively.

We note that only 13 plane waves are required for iMAP1 to yield the CNR compared with that of DAS with 75 transmissions. Fig. 6(a) and (b) show the images obtained by DAS from 13 and 75 transmissions. Images formed from 13 plane waves using iMAP1, iMAP2, Wiener postfilter, ScW, and CF are shown in Fig. 6(c)–(g), respectively.

4) Speckle Pattern: The similarity of speckle regions for images in Fig. 6 is evaluated using the K-S test as elaborated in Section VI-C. We use the DAS image with 75 transmissions as a reference. The similarity values are presented in Table III.

TABLE III
SIMILARITY OF SPECKLE REGIONS FOR DIFFERENT METHODS

Method	Simulation (Fig. 6), [%]	Experiment (Fig. 8), [%]
Wiener PF	63.36	70.50
iMAP1	74.12	90.02
iMAP2	62.45	61.26
ScW	25.10	24.00
CF	0.062	1.52

Evidently, the similarity of CF is extremely low; explicitly, less than 1% of the resulting pattern is defined as speckle by the K-S test. The first iteration of iMAP yields the highest similarity of 74.12%, while iMAP2 yields a similarity of 62.45% and is comparable to the Wiener postfilter. These results are in good agreement with the lateral cross section of the cyst phantom obtained with a single transmission presented in Fig. 4.

B. Experiments

We next proceed to the experimental data obtained by scanning a phantom containing both anechoic inclusions and a point reflector to allow for the evaluation of both contrast and resolution.

We start with the evaluation of contrast. Graphs of CR and CNR as a function of the number of plane waves are presented in Fig. 7. Similar to simulated data, the CNR of iMAP1 using 13 plane waves is comparable to that of DAS with 75 plane waves. Fig. 8(a) and (b) show the images obtained by DAS from 13 and 75 transmissions. Images formed with 13 plane waves using iMAP1, iMAP2, Wiener postfilter, ScW, and CF are shown in Fig. 8(c)–(g), respectively. Similar to simulation results, iMAP with one and two iterations and ScW provide prominent improvement of contrast. To take a closer look at the performance of the above-mentioned methods, lateral cross sections of upper and lower cysts of Fig. 8 are presented in Fig. 9(a) and (b), respectively. We note that all the techniques with 13 transmitted plane waves provide a sharper dropoff from speckle to cyst region compared with DAS with 75 transmissions. As in the simulated results, iMAP2 outperforms ScW in terms of noise suppression within the

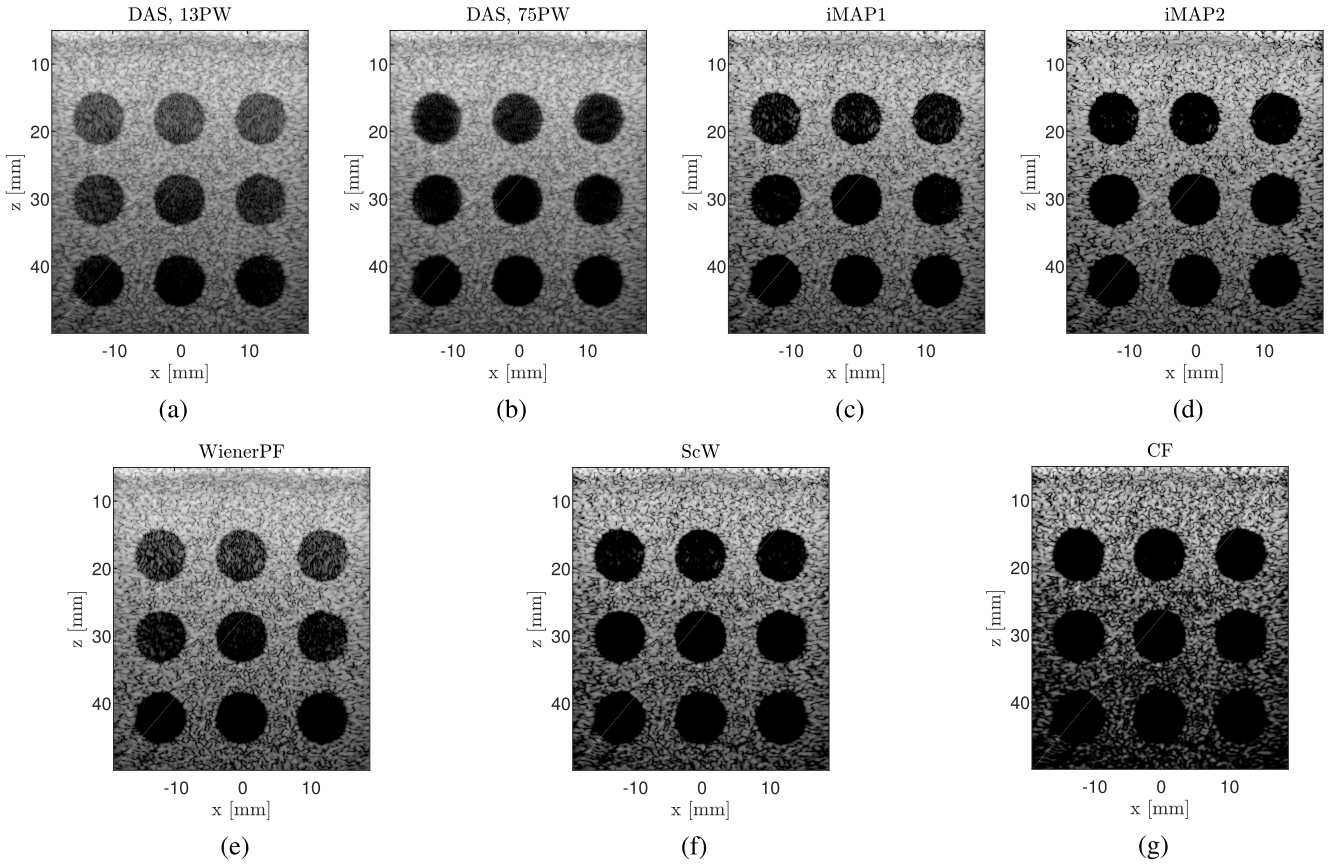

Fig. 6. Images of simulated anechoic cyst phantom obtained by (a) DAS with 13 plane waves, (b) DAS with 75 plane waves, (c) iMAP1 with 13 plane waves, (d) iMAP2 with 13 plane waves, (e) Wiener postfilter with 13 plane waves, (f) ScW with 13 plane waves, and (g) CF with 13 plane waves. All the images are presented with a dynamic range of 70 dB.

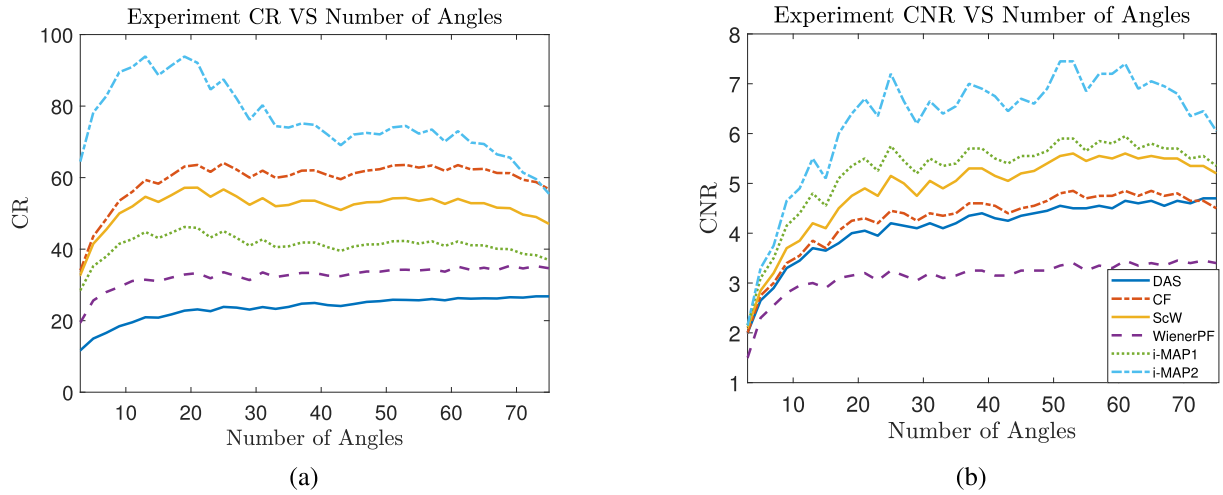

Fig. 7. (a) CR and (b) CNR as a function of the number of transmitted plane waves.

cyst while maintaining a speckle pattern that is closer to DAS the output. This is especially prominent for lower depth.

The quantitative measurements of contrast and lateral resolution of images in Fig. 8 are presented in Table IV. The axial resolution is 0.58 mm for all the images. It can be seen that iMAP1 with 13 plane waves is comparable to DAS based on 75 plane waves in terms of CR, CNR, and resolution. However, note that in terms of CSR, the performance of all the methods is reduced compared with DAS. This point is elaborated in Section VIII. Similarity values for speckle regions are presented in Table III. The DAS image with 75 transmissions is used as a reference.

The experimental results are in close agreement with simulations.

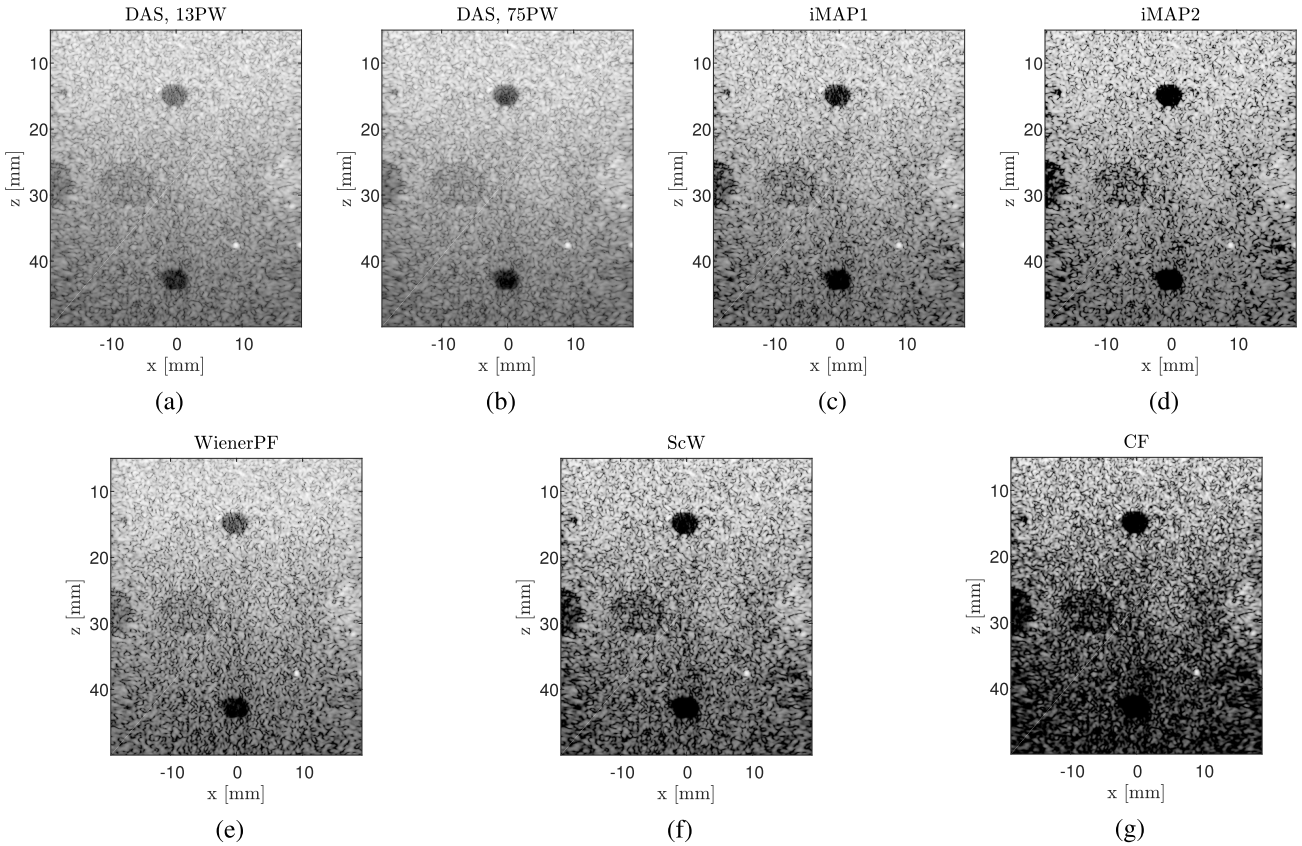

Fig. 8. Images of anechoic cyst phantom obtained by (a) DAS with 13 plane waves, (b) DAS with 75 plane waves, (c) iMAP1 with 13 plane waves, (d) iMAP2 with 13 plane waves, (e) Wiener postfilter with 13 plane waves, (f) ScW with 13 plane waves, and (g) CF with 13 plane waves. All the images are presented with a dynamic range of 70 dB.

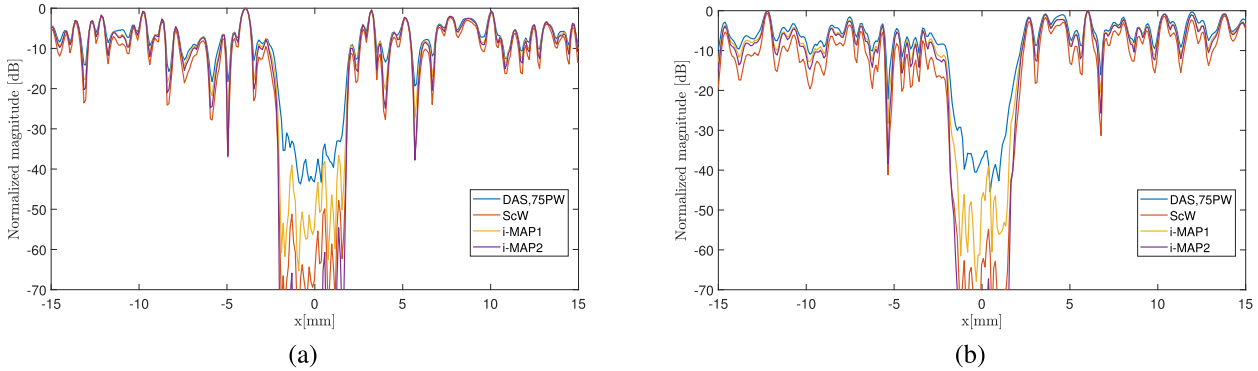

Fig. 9. Lateral cross section of the two cysts from Fig. 8. (a) Upper cyst. (b) Lower cyst. iMAP1, iMAP2, and ScW are using 13 transmitted plane waves. DAS is performed with 75 transmissions.

TABLE IV
MEASURED LATERAL RESOLUTION AND CONTRAST

Method	Lateral res. [mm]	CR[dB]	CNR [dB]	CSR [dB]
DAS, 13 PW	0.55	21	3.7	2.5
DAS, 75 PW	0.57	26.8	4.7	2.7
Wiener PF	0.41	31.5	3	1.7
iMAP1	0.55	44.8	4.8	2.3
ScW	0.51	54.7	4.2	2.4
CF	0.39	59.4	3.7	2.5
iMAP2	0.55	93.9	5.5	2.1

C. In Vivo Acquisition

Finally, we apply the proposed beamformer to two *in vivo* data sets of a carotid artery. Based on the results of Section VII-B, we compare DAS obtained with 13 and 75 transmissions with all the other methods. Figs. 10 and 11 show the cross section and the longitudinal scan of a carotid artery. The improvement of contrast is especially prominent in Fig. 10, where the cross section of the carotid artery is much cleaner with a very sharp edge for iMAP1, iMAP2, and ScW. To demonstrate the difference in the performance of the three above-mentioned techniques, Fig. 12 shows a lateral cross section of the carotid from Fig. 10 at a depth of 1.8 cm. We note that all the three methods with only 13 transmissions provide a sharper dropoff at the translation to the carotid cavity compared with DAS with 75 plane waves. In terms of clutter suppression within the artery, iMAP2 outperforms ScW; however, they both affect the speckle pattern. iMAP1 with 13 transmissions provides interference suppression comparable

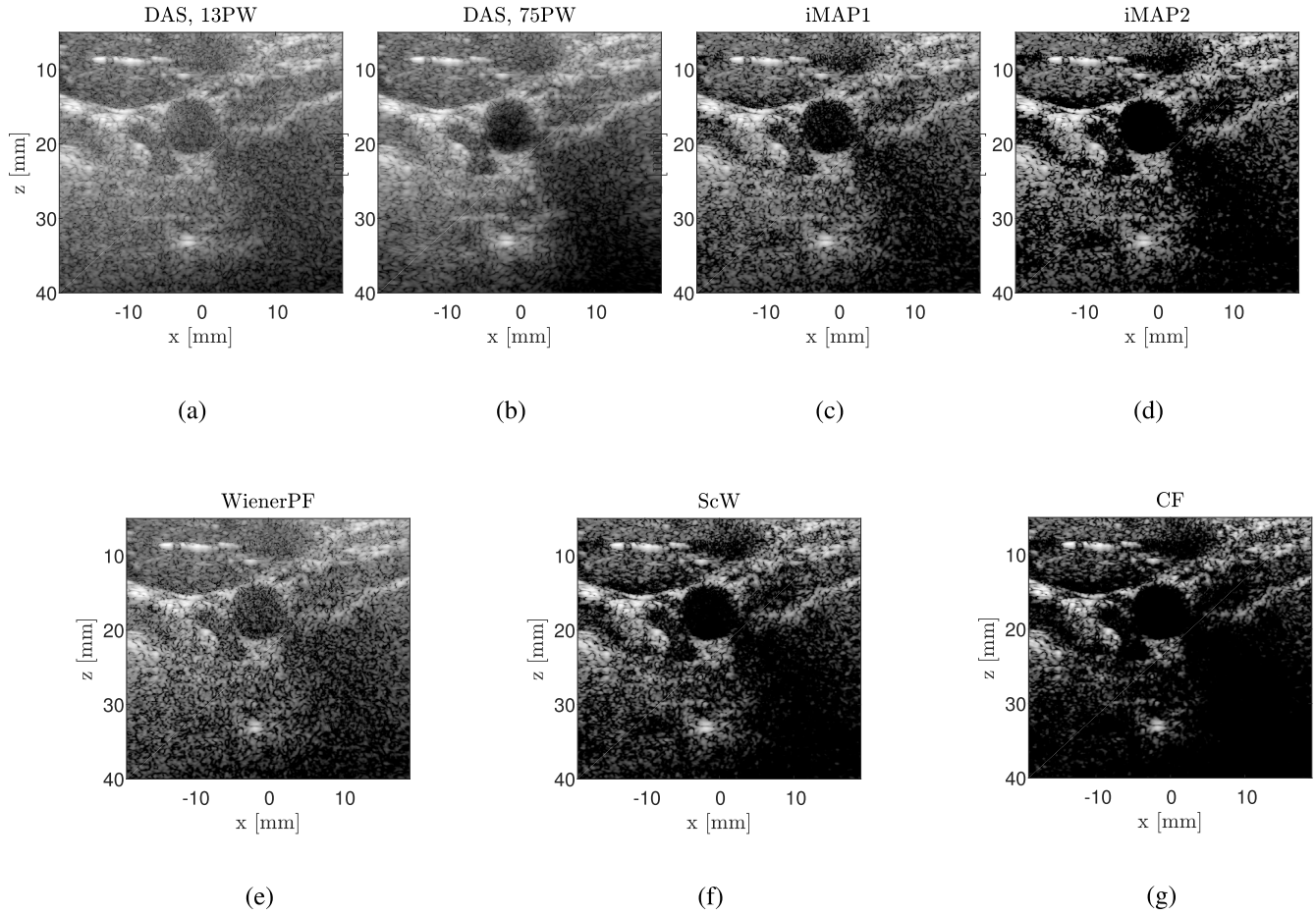

Fig. 10. Images of a cross section of a carotid artery obtained by (a) DAS with 13 plane waves, (b) DAS with 75 plane waves, (c) iMAP1 with 13 plane waves, (d) iMAP2 with 13 plane waves, (e) Wiener postfilter with 13 plane waves, (f) ScW with 13 plane waves, and (g) CF with 13 plane waves. All the images are presented with a dynamic range of 70 dB.

to DAS with 75 plane waves with much less effect on speckle regions compared with iMAP2 and ScW.

VIII. Discussion

The main effect of the interference suppression techniques, discussed in this article, is on image contrast. To evaluate the contrast properly and provide a thorough comparison of different methods, we used three contrast metrics, CR, CSR, and CNR, accepted in the literature. In Section VII, we saw that there are two kinds of discrepancies in the performance of the studied methods when different metrics are used. First, the improvement in CR is much more prominent compared with CNR. Second, the methods that outperform DAS in terms of CR and CNR perform equally or even slightly worse in terms of CSR. We now address the inconsistent values of different contrast metrics.

For both simulated and experimental data, all the examined methods outperform DAS in terms of CR. This implies that the mean value within the cyst is reduced due to interference suppression. Wiener postfilter and iMAP provide the CR improvement of above 44% and 108%, respectively. However, the CNR obtained with the Wiener postfilter is reduced compared with DAS for both simulated and experimental data. Moreover, there is a prominent gap between the performance improvement in terms of CR and CNR, e.g., iMAP1 and ScW provide more than 50% improvement in CR, while the improvement in CNR is only 7%–15%.

The above-mentioned phenomenon is explained by the increased variance of the background, which imposes a penalty on CNR. Comparison of CR and CNR shows that all the examined methods increase the variance of the background. These results are in agreement with the study of the effect of adaptive beamformers on speckle statistics presented recently in [33]. Hverven *et al.* [33] show that adaptive beamforming approaches such as MV and CF alter speckle statistics leading to more heavy-tailed distributions that result in increased variance. In general, the increased variance is undesirable and is a drawback of interference suppression. Statistical tests on the speckle region, performed in Section VII-A4, show that the similarity of the speckle region is reduced by all the methods, discussed in this article. However, the level of reduction varies greatly between different techniques: iMAP1 results in 90% similarity for experimental data, while CF yields only 1.52%.

The values of CSR for all the methods, except Wiener postfilter, are comparable to that of DAS. The fact that iMAP1 and iMAP2 do not show an advantage in terms of CSR compared with other approaches, as opposed to CR and CNR metrics, is explained by the increased variance within

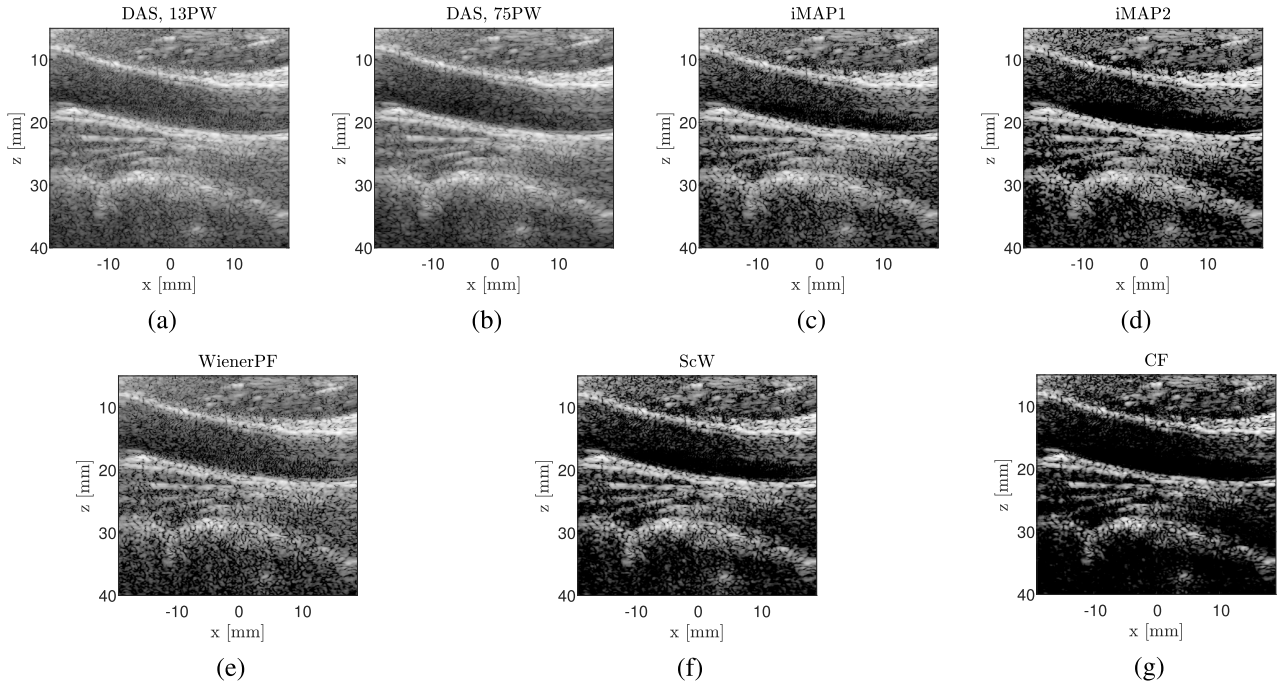

Fig. 11. Images of a longitudinal scan of a carotid artery obtained by (a) DAS with 13 plane waves, (b) DAS with 75 plane waves, (c) iMAP1 with 13 plane waves, (d) iMAP2 with 13 plane waves, (e) Wiener postfilter with 13 plane waves, (f) ScW with 13 plane waves, and (g) CF with 13 plane waves. All the images are presented with a dynamic range of 70 dB.

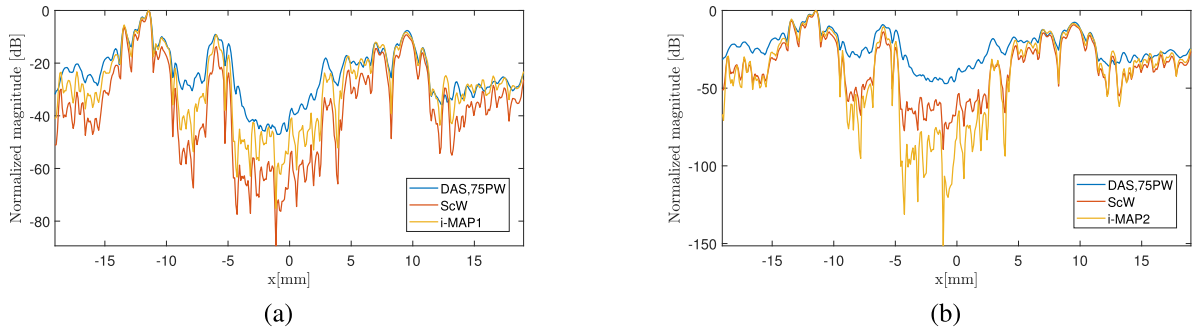

Fig. 12. Lateral cross section of the carotid from Fig. 10. (a) iMAP1 and ScW. (b) iMAP2 and ScW. iMAP1, iMAP2, and ScW are using 13 transmitted plane waves. DAS is performed with 75 transmissions.

the cyst. To put it explicitly, iMAP1 and iMAP2 yield reduced mean value within the cyst compared with Wiener postfilter and CF and ScW, respectively, while keeping the increase in background variance moderate. This can be seen from the values of CR and CNR as well as in Fig. 4. The increase in variance within the cyst, however, is higher for iMAP, leading to lower values of CSR.

As mentioned in Section VII-A2, CR, CSR, and CNR are accepted quantitative contrast metrics. Recently, an alternative approach for contrast analysis was proposed in [33]. The authors used simulated data to show that some adaptive beamforming methods tend to stretch the dynamic range of the image. This results in misleading improvement of measured resolution and contrast. Rindal *et al.* [33] propose to use dynamic range calibration (DRC) to compensate for the differences and allow for a fair comparison. Interestingly, the differences between CR before and after DRC resemble the gaps between CR and CNR we observed in our experiments. This may indicate that the penalty on increased background variance applied by CNR, accounts, to some extent, for a stretched dynamic range of the image.

The metrics for contrast evaluation provide meaningful insights into the performance of different methods and help to pinpoint their benefits and limitations. However, the resulting numbers are not always informative. As we can see here, the improved difference between the mean values of cyst and background is canceled by the increased variance within the cyst. This results in the close values of CSR, while the resulting images are very different. On the other hand, CR alone can also be misleading since it is insensitive to changes in the variance of neither background nor the region of interest. It is, therefore, important to analyze several contrast metrics together with the resulting images and even cross section of regions being studied. Moreover, the relationship between quantitative metrics of contrast, its qualitative perception, as well as the effects on dynamic range and statistical

properties of speckle should be further studied and linked together to allow for study and fair comparison of different beamforming techniques.

IX. Conclusion

In this work, we proposed a statistical interpretation of the beamforming process. We treat the signal of interest and the interference as uncorrelated Gaussian random variables and view beamforming as MAP estimation of the signal of interest. The implementation of MAP requires the knowledge of the signal and interference variances. We propose using the current estimator of the signal of interest to improve the estimation of the distribution parameters and vice versa, leading to an iterative implementation of the MAP beamformer. The resulting iterative scheme is computationally simple and does not require fine-tuning of parameters.

The proposed method improves the contrast in terms of CR and CNR compared with DAS as demonstrated using both simulated and experimental data. Only 13 plane waves are required for iMAP1 to obtain the CNR of DAS with 75 transmissions. The second iteration, iMAP2, leads to 80–100-dB noise suppression inside the cyst regions. The comparison of Wiener postfilter, CF, and ScW with the signal model and parameter estimators proposed in previous works shows the superior performance of iMAP in terms of CR and CNR and better preserved speckle patterns, which is verified by a statistical K-S test. A study of CR, CNR, and CSR shows that iMAP1 and iMAP2 yield a reduced mean value within the cyst compared with Wiener postfilter and CF and ScW, respectively, while keeping the increase in background variance moderate. However, the increase in variance within the cyst is more prominent for iMAP.

In this work, we proposed and implemented an algorithm based on a simple, yet, reasonable model. Our approach shows the ability to suppress interference without significantly increasing complexity. Obviously, studying more involved models is of interest since this can potentially further improve performance. We note, however, that the comparison of Wiener postfilter and iMAP performance points to a tradeoff between the correctness of the model and the ability to estimate its parameters. We can consider iMAP and the Wiener postfilter as two extreme cases: iMAP is based on a simple model that requires the estimation of only two parameters: the variances of the signal of interest and the noise. In contrast, the Wiener postfilter does not make any assumptions on the noise distribution. As a result, the model is much more general but it requires estimating the entire noise covariance matrix. The empirical results presented in this article show that iMAP outperforms Wiener postfilter in terms of contrast. This can be explained by a poor estimation of the noise covariance matrix. A detailed study of more involved models and their effect on parameter estimation is left to future work.

In addition to quantitative measurements, based on simulated and experimental phantoms, two *in vivo* scans allow for the visual assessment of the resulting image quality. The *in vivo* results are consistent with simulations and phantom scans in terms of contrast improvement. However, one can note that the background brightness is reduced in the vicinity of hyperechoic regions, as it appears in Fig. 10 (c), (d), (f), and (g) above the carotid cross section on the right side of the hyperechoic structure. This artifact is seen in the images obtained by iMAP, ScW, and CF. All the above exploit the assumption of spatially white interference. This is not the case in a hyperechoic region that contaminates the signal detected by the elements in a highly correlated manner. To cope with this problem, the correlation between detected signals should be taken into account, leading to an improved estimation of signal and noise variances.

To conclude, iMAP provides a prominent improvement of contrast without affecting the resolution and results in a speckle pattern comparable to that of DAS. Consequently, for the plane-wave mode, fewer transmissions are required, maintaining high frame rate and reducing the amount of computations. The achieved improvement in image quality while keeping high frame rate makes the proposed method appealing to ultrafast modalities such as coherent plane-wave elastography [19] and ultrafast Doppler [34].

References

[1] M. Tanter and M. Fink, "Ultrafast imaging in biomedical ultrasound," *IEEE Trans. Ultrason., Ferroelectr., Freq. Control*, vol. 61, no. 1, pp. 102–119, Jan. 2014.

[2] J. Capon, "High-resolution frequency-wavenumber spectrum analysis," *Proc. IEEE*, vol. 57, no. 8, pp. 1408–1418, Aug. 1969.

[3] J. A. Mann and W. F. Walker, "A constrained adaptive beamformer for medical ultrasound: Initial results," in *Proc. IEEE Ultrason. Symp.*, vol. 2, Oct. 2002, pp. 1807–1810.

[4] M. Sasso and C. Cohen-Bacrie, "Medical ultrasound imaging using the fully adaptive beamformer," in *Proc. IEEE Int. Conf. Acoust., Speech, Signal Process. (ICAASP)*, vol. 2, Mar. 2005, pp. 489–492.

[5] J. F. Synnevag, A. Austeng, and S. Holm, "Adaptive beamforming applied to medical ultrasound imaging," *IEEE Trans. Ultrason., Ferroelectr., Freq. Control*, vol. 54, no. 8, pp. 1606–1613, Aug. 2007.

[6] F. Vignon and M. R. Burcher, "Capon beamforming in medical ultrasound imaging with focused beams," *IEEE Trans. Ultrason., Ferroelectr., Freq. Control*, vol. 55, no. 3, pp. 619–628, Mar. 2008.

[7] A. Austeng, C.-I. C. Nilsen, A. C. Jensen, S. P. Näsholm, and S. Holm, "Coherent plane-wave compounding and minimum variance beamforming," in *Proc. IEEE Int. Ultrason. Symp. (IUS)*, Oct. 2011, pp. 2448–2451.

[8] N. Q. Nguyen and R. W. Prager, "Minimum variance beamformers for coherent plane-wave compounding," *Proc. SPIE*, vol. 10139, Mar. 2017, Art. no. 1013912.

[9] R. Mallart and M. Fink, "Adaptive focusing in scattering media through sound-speed inhomogeneities: The van Cittert Zernike approach and focusing criterion," *J. Acoust. Soc. Amer.*, vol. 96, no. 6, pp. 3721–3732, 1994.

[10] K. W. Hollman, K. W. Rigby, and M. O'Donnell, "Coherence factor of speckle from a multi-row probe," in *Proc. IEEE Ultrason. Symp.*, vol. 2, Oct. 1999, pp. 1257–1260.

[11] M.-K. Jeong, "A Fourier transform-based sidelobe reduction method in ultrasound imaging," *IEEE Trans. Ultrason., Ferroelectr., Freq. Control*, vol. 47, no. 3, pp. 759–763, May 2000.

[12] P.-C. Li and M.-L. Li, "Adaptive imaging using the generalized coherence factor," *IEEE Trans. Ultrason., Ferroelectr., Freq. Control*, vol. 50, no. 2, pp. 128–141, Feb. 2003.

[13] S.-L. Wang, C.-H. Chang, H.-C. Yang, Y.-H. Chou, and P.-C. Li, "Performance evaluation of coherence-based adaptive imaging using clinical breast data," *IEEE Trans. Ultrason., Ferroelectr., Freq. Control*, vol. 54, no. 8, pp. 1669–1679, Aug. 2007.

[14] B. M. Asl and A. Mahloojifar, "Minimum variance beamforming combined with adaptive coherence weighting applied to medical ultrasound imaging," *IEEE Trans. Ultrason., Ferroelectr., Freq. Control*, vol. 56, no. 9, pp. 1923–1931, Oct. 2009.

[15] M. Xu, Y. Chen, M. Ding, and M. Yuchi, "Adaptive minimum variance beamforming combined with phase coherence imaging for ultrasound imaging," *Proc. SPIE*, vol. 8320, Feb. 2012, Art. no. 83200E.

[16] S.-L. Wang and P.-C. Li, "MVDR-based coherence weighting for high-frame-rate adaptive imaging," *IEEE Trans. Ultrason., Ferroelectr., Freq. Control*, vol. 56, no. 10, pp. 2097–2110, Oct. 2009.
[17] C.-I. C. Nilsen and S. Holm, "Wiener beamforming and the coherence factor in ultrasound imaging," *IEEE Trans. Ultrason., Ferroelectr., Freq. Control*, vol. 57, no. 6, pp. 1329–1346, Jun. 2010.
[18] H. L. van Trees, *Detection, Estimation, and Modulation Theory*. Hoboken, NJ, USA: Wiley, 2004.
[19] G. Montaldo, M. Tanter, J. Bercoff, N. Benech, and M. Fink, "Coherent plane-wave compounding for very high frame rate ultrasonography and transient elastography," *IEEE Trans. Ultrason., Ferroelectr., Freq. Control*, vol. 56, no. 3, pp. 489–506, Mar. 2009.
[20] J. Zhao, Y. Wang, J. Yu, W. Guo, T. Li, and Y.-P. Zheng, "Subarray coherence based postfilter for eigenspace based minimum variance beamformer in ultrasound plane-wave imaging," *Ultrasonics*, vol. 65, pp. 23–33, Feb. 2016.
[21] B. P. Carlin and T. A. Louis, *Bayes and Empirical Bayes Methods for Data Analysis*, vol. 17. Boca Raton, FL, USA: CRC Press, 2000.
[22] H. Liebgott, A. Rodriguez-Molares, F. Cervenansky, J. A. Jensen, and O. Bernard, "Plane-wave imaging challenge in medical ultrasound," in *Proc. IEEE Int. Ultrason. Symp. (IUS)*, Sep. 2016, pp. 1–4.
[23] G. F. Pinton, G. E. Trahey, and J. J. Dahl, "Spatial coherence in human tissue: Implications for imaging and measurement," *IEEE Trans. Ultrason., Ferroelectr., Freq. Control*, vol. 61, no. 12, pp. 1976–1987, Dec. 2014.
[24] J. A. Jensen and N. B. Svendsen, "Calculation of pressure fields from arbitrarily shaped, apodized, and excited ultrasound transducers," *IEEE Trans. Ultrason., Ferroelectr., Freq. Control*, vol. 39, no. 2, pp. 262–267, Mar. 1992.
[25] J. A. Jensen, "FIELD: A program for simulating ultrasound systems," in *Proc. IEEE 10th Nordic-Baltic Conf. Biomed. Imag.*, vol. 34, Mar. 1996, pp. 351–353.
[26] Y. Notomi *et al.*, "Measurement of ventricular torsion by two-dimensional ultrasound speckle tracking imaging," *J. Amer. College Cardiol.*, vol. 45, no. 12, pp. 2034–2041, 2005.
[27] E. Harris, N. R. Miller, J. C. Bamber, J. R. N. Symonds-Tayler, and P. M. Evans, "Speckle tracking in a phantom and feature-based tracking in liver in the presence of respiratory motion using 4D ultrasound," *Phys. Med. Biol.*, vol. 55, no. 12, p. 3363, 2010.
[28] D. H. Turnbull, P. K. Lum, A. T. Kerr, and F. S. Foster, "Simulation of B-scan images from two-dimensional transducer arrays: Part I—Methods and quantitative contrast measurements," *Ultrason. Imag.*, vol. 14, no. 4, pp. 323–343, 1992.
[29] M. S. Patterson and F. S. Foster, "The improvement and quantitative assessment of B-mode images produced by an annular array/cone hybrid," *Ultrason. Imag.*, vol. 5, no. 3, pp. 195–213, 1983.
[30] S. Krishnan, K. W. Rigby, and M. O'Donnell, "Improved estimation of phase aberration profiles," *IEEE Trans. Ultrason., Ferroelectr., Freq. Control*, vol. 44, no. 3, pp. 701–713, May 1997.
[31] C. B. Burckhardt, "Speckle in ultrasound B-mode scans," *IEEE Trans. Sonics Ultrason.*, vol. SU-25, no. 1, pp. 1–6, Jan. 1978.
[32] R. F. Wagner, S. W. Smith, J. M. Sandrik, and H. Lopez, "Statistics of speckle in ultrasound B-scans," *IEEE Trans. Sonics Ultrason.*, vol. SU-30, no. 3, pp. 156–163, May 1983.
[33] S. M. Hverven, O. M. H. Rindal, A. Rodriguez-Molares, and A. Austeng, "The influence of speckle statistics on contrast metrics in ultrasound imaging," in *Proc. IEEE Int. Ultrason. Symp. (IUS)*, Sep. 2017, pp. 1–4.
[34] J. Bercoff *et al.*, "Ultrafast compound Doppler imaging: Providing full blood flow characterization," *IEEE Trans. Ultrason., Ferroelectr., Freq. Control*, vol. 58, no. 1, pp. 134–147, Jan. 2011.

Tanya Chernyakova received the B.Sc. degree in biomedical engineering and the Ph.D. degree in electrical engineering from the Technion-Israel Institute of Technology, Haifa, Israel, for her research in low-rate generalized beamforming for medical ultrasound.

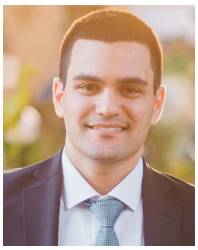

Dan Cohen received the B.S. degree in electrical engineering from Technion, Haifa, Israel, in 2017. He is currently pursuing the M.Sc. degree with the Department of Electrical Engineering, Technion Israel Institute of Technology, Haifa.

His research interests include computer vision and deep learning.

Meged Shoham received the B.S. degree in electrical engineering from Technion, Haifa, Israel, in 2017. He is currently pursuing the M.Sc. degree with the Department of Electrical Engineering, Technion Israel Institute of Technology, Haifa.

His research interests include computer graphics and computer vision.

Yonina C. Eldar (S'98–M'02–SM'07–F'12) received the B.Sc. degree in physics and the B.Sc. degree in electrical engineering from Tel-Aviv University (TAU), Tel-Aviv, Israel, in 1995 and 1996, respectively, and the Ph.D. degree in electrical engineering and computer science from the Massachusetts Institute of Technology (MIT), Cambridge, MA, USA, in 2002.

She is currently a Professor with the Department of Mathematics and Computer Science, Weizmann Institute of Science, Rechovot, Israel. She was previously a Professor at the Department of Electrical Engineering, Technion, Haifa, Israel, where she held the Edwards Chair in Engineering. She is also a Visiting Professor at MIT, a Visiting Scientist at the Broad Institute, an Adjunct Professor at Duke University, Durham, NC, USA, and was a Visiting Professor at Stanford. She is the author of the book *Sampling Theory: Beyond Bandlimited Systems* (Cambridge University Press) and coauthor of the books *Compressed Sensing* (Cambridge University Press) and *Convex Optimization Methods in Signal Processing and Communications* (Cambridge University Press). Her research interests are in the broad areas of statistical signal processing, sampling theory and compressed sensing, learning, and optimization methods and their applications to biology and optics.

Dr. Eldar was a member of the Young Israel Academy of Science and Humanities and the Israel Committee for Higher Education. She was a Horev Fellow of the Leaders in Science and Technology Program at the Technion and an Alon Fellow. She is a member of the Israel Academy of Sciences and Humanities (elected 2017), and a fellow of EURASIP. She has received many awards for excellence in research and teaching, including the IEEE Signal Processing Society Technical Achievement Award (2013), the IEEE/AESS Fred Nathanson Memorial Radar Award (2014), and the IEEE Kiyo Tomiyasu Award (2016). She received the Michael Bruno Memorial Award from the Rothschild Foundation, the Weizmann Prize for Exact Sciences, the Wolf Foundation Krill Prize for Excellence in Scientific Research, the Henry Taub Prize for Excellence in Research (twice), the Hershel Rich Innovation Award (three times), the Award for Women with Distinguished Contributions, the Andre and Bella Meyer Lectureship, the Career Development Chair at the Technion, the Muriel & David Jacknow Award for Excellence in Teaching, and the Technion's Award for Excellence in Teaching (two times). She received several best paper awards and best demo awards together with her research students and colleagues, including the SIAM Outstanding Paper Prize, the UFFC Outstanding Paper Award, the Signal Processing Society Best Paper Award, and the IET Circuits, Devices and Systems Premium Award. She was selected as one of the 50 most influential women in Israel. She was the co-chair and technical co-chair of several international conferences and workshops. She is the Editor-in-Chief of the *Foundations and Trends in Signal Processing*, a member of the IEEE Sensor Array and Multichannel Technical Committee and serves on several other IEEE committees. In the past, she was a Signal Processing Society Distinguished Lecturer, a member of the IEEE Signal Processing Theory and Methods and Bio-Imaging Signal Processing technical committees, and served as an Associate Editor for the IEEE TRANSACTIONS ON SIGNAL PROCESSING, the *EURASIP Journal of Signal Processing*, the *SIAM Journal on Matrix Analysis and Applications*, and the *SIAM Journal on Imaging Sciences*.